# Time-Resolved Raman Spectrometer With High Fluorescence Rejection Based on a CMOS SPAD Line Sensor and a 573-nm Pulsed Laser

Tuomo Talala⬤, Ville A. Kaikkonen⬤, Pekka Keränen⬤, *Member, IEEE*, Jari Nikkinen⬤, Antti Härkönen⬤, Vasili G. Savitski⬤, Sean Reilly⬤, Łukasz Dziechciarczyk⬤, Alan J. Kemp⬤, *Member, IEEE*, Mircea Guina⬤, *Member, IEEE*, Anssi J. Mäkynen⬤, and Ilkka Nissinen⬤, *Member, IEEE*

*Abstract*—A time-resolved Raman spectrometer is demonstrated based on a 256 × 8 single-photon avalanche diodes fabricated in CMOS technology (CMOS SPAD) line sensor and a 573-nm fiber-coupled diamond Raman laser delivering pulses with duration below 100-ps full-width at half-maximum (FWHM). The collected backscattered light from the sample is dispersed on the line sensor using a custom volume holographic grating having 1800 lines/mm. Efficient fluorescence rejection in the Raman measurements is achieved due to a combination of time gating on sub-100-ps time scale and a 573-nm excitation wavelength. To demonstrate the performance of the spectrometer, fluorescent oil samples were measured. For organic sesame seed oil having a continuous wave (CW) mode fluorescence-to-Raman ratio of 10.5 and a fluorescence lifetime of 2.7 ns, a signal-to-distortion value of 76.2 was achieved. For roasted sesame seed oil having a CW mode fluorescence-to-Raman ratio of 82 and a fluorescence lifetime of 2.2 ns, a signal-to-distortion value of 28.2 was achieved. In both cases, the fluorescence-to-Raman ratio was reduced by a factor of 24–25 owing to time gating. For organic oil, spectral distortion was dominated by dark counts, while for the more fluorescent roasted oil, the main source of spectral distortion was timing skew of the sensor. With the presented postprocessing techniques, the level of distortion could be reduced by 88%–89% for both samples. Compared with common 532-nm excitation, approximately 73% lower fluorescence-to-Raman ratio was observed for 573-nm excitation when analyzing the organic sesame seed oil.

Tuomo Talala, Pekka Keränen, and Ilkka Nissinen are with the Circuits and Systems Research Unit, University of Oulu, 90014 Oulu, Finland (e-mail: tuomo.talala@oulu.fi).

Ville A. Kaikkonen and Anssi J. Mäkynen are with the Optoelectronics and Measurement Techniques Research Unit, University of Oulu, 90014 Oulu, Finland.

Jari Nikkinen, Antti Härkönen, and Mircea Guina are with the Optoelectronics Research Centre, Physics Unit, Tampere University, 33720 Tampere, Finland.

Vasili G. Savitski is with the Fraunhofer Centre for Applied Photonics, Fraunhofer UK Research Ltd., Glasgow G1 1RD, U.K.

Sean Reilly, Łukasz Dziechciarczyk, and Alan J. Kemp are with the Department of Physics, Institute of Photonics, SUPA, University of Strathclyde, Glasgow G1 1RD, U.K.

Digital Object Identifier 10.1109/TIM.2021.3054679

## I. INTRODUCTION

**R**AMAN spectroscopy is used in a wide range of fields including food and oil industries, mining industry, medical diagnostics, pharmacy, forensic science, and archaeometry [1]–[9]. In many applications, the largest challenge for Raman spectroscopy is fluorescence. For a wide range of samples, the illumination aimed at Raman excitation also induces strong fluorescence emission which masks weaker Raman scattering partially or completely. To this end, a number of methods have been developed to reduce the fluorescence problem. Techniques including surface-enhanced Raman spectroscopy and resonance Raman spectroscopy have been used to amplify Raman scattering, and, for example, infrared excitation, photobleaching, and quenching agents have been used to decrease fluorescence emission [10]–[14].

If traditional continuous wave (CW) excitation is used, both Raman scattering and fluorescence emission are observed continuously, and they cannot be separated in the time domain. As Raman scattering occurs nearly instantly but fluorescence has typically a lifetime in a range of nanoseconds to microseconds, pulsed excitation and time-gated measurement can be used to decrease the number of detected fluorescence photons. Time-gated Raman spectrometers have been built based on optical gates (Kerr, Pockels) [15], [16], time-gated photomultiplier tubes [17], streak cameras [18], intensified charge-coupled devices [15], and time-gated single-photon avalanche diodes fabricated in CMOS technology (CMOS SPADs) [19]. To achieve effective fluorescence rejection by means of time gating, the pulsewidth of the excitation laser should be as short as possible compared with the fluorescence lifetime of the sample to be measured [17]. The best signal-to-noise ratio is then reached with a gate width that is 1–2 times the width [full-width at half-maximum (FWHM)] of Raman photon distribution [17], [20]. The exact optimal gate width depends on the properties of the sample (fluorescence level and lifetime) and the sensor [dark count rate (DCR), timing skew].

In CMOS technology, the electronics needed for time-gated measurement or for time-correlated single-photon counting

can be integrated on the same chip with the SPADs. Because of that, a CMOS SPAD line sensor offers a compact solution for time-gated Raman spectroscopy and several such sensors have been demonstrated [21]–[23]. The timing jitter of a CMOS SPAD is typically in the range of 50–100 ps (FWHM) [24]–[27]. Therefore, the temporal resolution of approximately 50 ps in the latest CMOS SPAD line sensors is good enough to form relevant gate widths for Raman photon distributions detected with CMOS SPADs. However, when highly fluorescent samples are measured with CMOS SPAD line sensors, the dominant error source distorting the Raman spectrum is no longer shot noise from fluorescence but the timing skew of the line sensor [28], [29]. Therefore, when a CMOS SPAD line sensor is used for time-gated Raman measurement, good temporal resolution is not only needed to set proper time gating, but also to characterize and compensate for the timing skew of the sensor. In fact, the temporal resolution requirements might be stricter for the latter purpose.

In previous studies, CMOS SPAD line sensors have been used mostly with 532-nm pulsed lasers having pulsewidths of 150–400 ps (FWHM) [22], [23], [30], [31]. Compared with longer infrared wavelengths, 532-nm excitation gives a stronger Raman signal as the intensity of Raman scattering is inversely proportional to fourth power of excitation wavelength. Also, the photon detection efficiency of a SPAD is typically higher at visible wavelengths compared with the near infrared region [25]–[27]. One obvious weakness for 532-nm excitation is its tendency to produce stronger fluorescence emission than near infrared excitation. Although this ground rule of fluorescence decreasing as excitation wavelength increases is usually correct for large changes in wavelength (comparison between visible light and near infrared excitation), smaller changes in excitation wavelength can either decrease or increase fluorescence emission [32], [33]. One important point is that if the excitation wavelength is changed, wavelengths for Raman scattering also change but fluorescence emission wavelengths are not shifted. Therefore, if the excitation wavelength can be chosen, this selection can be used to set Raman peaks to a wavelength range that has the least fluorescence. This way, a Raman spectrometer can be optimized for a certain kind of samples.

Raman spectra of samples containing human blood have been measured for various purposes, to detect diseases and to monitor the glucose level of blood, for example [34]. Fluorescence emission from hemoglobin is high for the excitation wavelengths in the range of 525–580 nm and it decreases rapidly, if excitation is shifted to around 600 nm or above. To minimize the fluorescence emission, a 599-nm $Ba(NO_3)_2$ crystal-based Raman shifting laser has been used with blood samples [35]. Another example of an organic sample showing significant fluorescence emission is olive oil, which Raman spectra have been measured to detect oil adulterations [4]. Over the range of 500–750 nm, its fluorescence emission is lowest at 620–640 nm [33]. In addition, over the range of 300–680 nm, its fluorescence absorption is lowest at 570–590 nm. Thus, to measure the Raman spectrum of olive oil, excitation wavelength between 570 and 590 nm could be better choice than standard 532 nm. More generally, excitation

wavelength between 570 and 590 nm could be good choice if samples containing other edible oils, biodiesel, or diesel are measured [36]. For both examples above, a very suitable excitation wavelength can be produced with a diamond Raman laser: 573 nm for samples containing oils and 620 nm for samples including hemoglobin [37], [38].

In this article, the design, the implementation, and the performance of a new time-resolved Raman spectrometer are presented. The instrument is built around a 256-channel time-resolved CMOS SPAD line sensor and a 573-nm pulsed laser. The main aim is to show the effectiveness of a 573-nm wavelength and a sub-100-ps pulsewidth together with a time-resolved CMOS SPAD line sensor on the fluorescence rejection with oil samples. While the overall fluorescence level decrease is achieved by the proper excitation wavelength used, the main rejection of fluorescence is enabled by the accurate time-correlated single-photon counting of the sensor with a sub-100-ps laser pulses. The temporal resolution of the sensor, 20 ps, enables accurate time gating for fluorescence rejection in data postprocessing. In addition, due to high temporal resolution, it is possible to perform precise timing skew characterization and compensation for the sensor. With a new improved timing skew characterization method, the effective timing skew after the compensation is pushed down to picosecond level revealing Raman spectra of highly fluorescent samples that would not otherwise be visible. The structure of the spectrometer is described in Section II, the calibration procedure and calibration measurement results are shown in Section III, performance of the spectrometer and postprocessing methods are demonstrated with measurement results in Section IV, and Section V concludes this article.

## II. STRUCTURE OF THE SPECTROMETER

A flowchart of the spectrometer design is shown in Fig. 1. Colors of arrows in the flowchart approximately correspond to light wavelengths at particular sections of the spectrometer. Electronic signals are drawn in gray. Collimators and focusing lenses are not included.

The excitation source is a diamond Raman laser that consists of a 532-nm pump laser and a 0.5-mm-thick synthetic diamond with integrated mirror coatings to form a plane-plane laser resonator. The first Stokes emission line from the diamond at 573 nm is used as the excitation light source to illuminate the sample in spectrometer. The laser exhibits a maximum average output power of 175 mW with a pulsewidth of 71 ps at 573 nm [37]. When used in the spectrometer, the current to the pump laser was adjusted so that the average output power at 573 nm was approximately 25 mW. At 25-mW power level, the measured pulsewidth was in a range of 70–100 ps (FWHM) and the pulse rate was 70 kHz. A detailed description of the laser can be found in [37].

At first, on the optical path, the output of the laser is filtered with a 550-nm long-pass filter to remove lower wavelength anti-Stokes emissions from the diamond. Then, 3% of the optical power is split to a light detector for synchronization signal generation and 97% of the power is coupled into a 5-m-long graded-index multimode optical fiber with 62.5 micron core
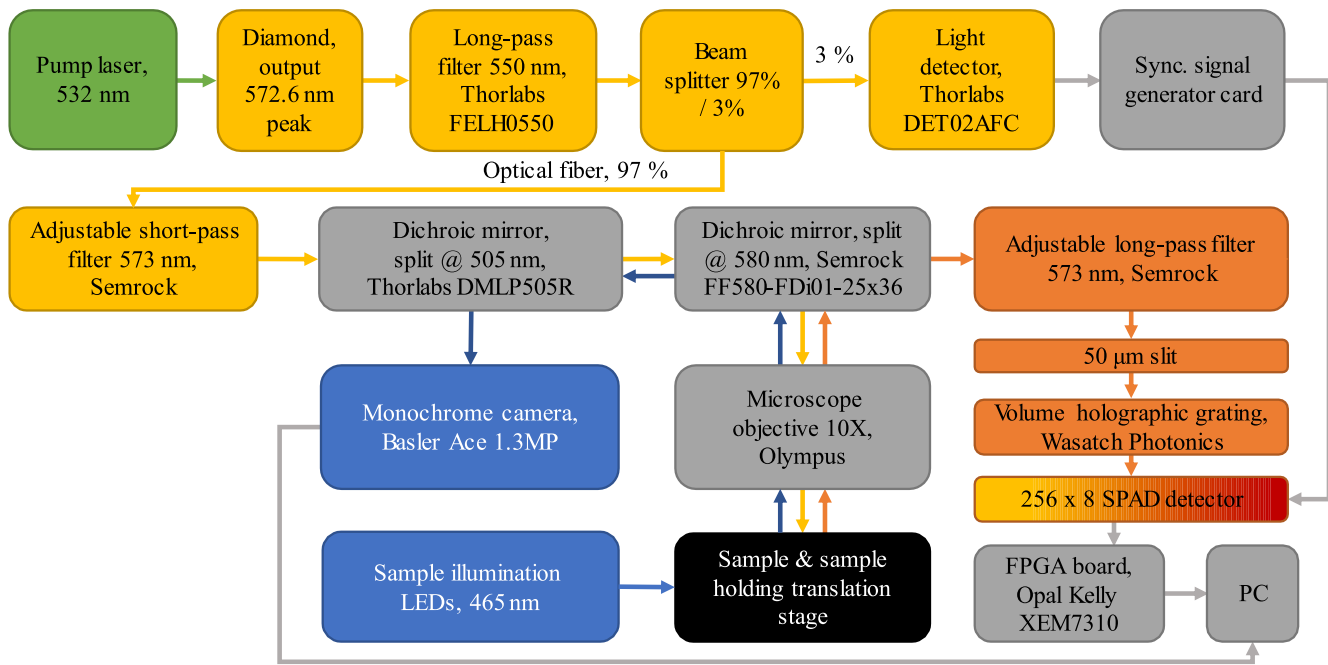
Fig. 1. Flowchart of the spectrometer. Collimators and focusing lenses are ignored.

diameter to generate a long enough optical delay for the synchronization with the line sensor. Although a graded-index fiber has larger attenuation for the 573-nm wavelength, it has smaller modal dispersion than a similar sized step-index fiber and is, therefore, used in the spectrometer. From the optical fiber, the excitation light is collimated using a 11-mm focal length lens (CFC-11X-A, Thorlabs) and directed toward the sample through a 573-nm short-pass filter, two long-pass dichroic mirrors, and focused on the sample using a $10\times/0.25$ microscope objective. The adjustable 573-nm short-pass filter is used to remove higher order Stokes emissions generated in the diamond and fiber. The first dichroic (DMLP505R, Thorlabs) transmits the 573-nm excitation and reflects the lower wavelength light to the camera, which is used for imaging purposes. A 580-nm wavelength long-pass dichroic mirror (FF580-FDi01-25 $\times$ 36, Semrock), angled at 45° to the excitation beam, reflects the excitation beam to the microscope objective and on to the sample. The microscope objective collects the Raman and the fluorescence light scattered at 180° from the sample, as well as the Rayleigh scattered excitation light. The same dichroic then transmits the Stokes Raman and fluorescence light and reflects most of the excitation light. After the dichroic, the collected light is passed through an additional 573-nm long-pass filter to remove the residual excitation light remaining after the dichroic. The long-pass filtered light is focused using a 100-mm focal length lens on a 50-$\mu$m wide slit. The light that passes through the slit is collimated using an 85-mm f/1.4 camera objective to a custom volume holographic grating with 1800 lines/mm (Wasatch Photonics). An identical camera objective focuses the dispersed light from the grating on the line detector. The optical magnification from the microscope objective object plane to the line detector image plane is $5.6\times$, and the spot size of the excitation light on the sample is 110 $\mu$m in diameter by geometrical approximation.

The light detector (Thorlabs DET02AFC) creates a short analog synchronization signal from a laser pulse. This signal is then converted into a longer logic-level signal on a custom designed synchronization signal generator card. This logic-level signal is connected to the detector to synchronize measurements with the laser pulses.

The detector of the spectrometer is a time-resolved 256-channel SPAD line sensor fabricated in 0.35-$\mu$m CMOS technology. Each channel contains eight SPADs arranged in vertical direction and a time-to-digital converter (TDC) with a resolution and range of 20 ps and 640 ns, respectively. The diameter of SPAD's active area and the pitch in SPAD array are 25.6 and 41.6 $\mu$m, respectively. The fill factor of the whole array is about 35%. Although the detector has been designed primarily for a line profiling laser radar, high temporal resolution and good uniformity between channels make it very suitable for time-resolved Raman spectroscopy. As the range of TDCs is much wider than needed for Raman spectroscopy, only the first 4096 TDC bins (81.92 ns range) were used in the Raman measurements. For communication between the detector and a computer, a field-programmable gate array (FPGA) integration board (Opal Kelly XEM7310) is used. Full characterization for the detector is presented in [39] and [40].

The wavelength range covered by the line sensor was 580.8–639.5 nm, corresponding to a wavenumber range of 247–1826 cm$^{-1}$. This wavenumber range divided by the 256 channels of the detector gives a theoretical spectral resolution of 6.2 cm$^{-1}$. As an example, raw data from sesame seed oil measurements (for TDC bins 400–800) are shown in Fig. 2.

To make focusing of the excitation easier and more accurate, the sample was monitored through the microscope objective with a Basler ace monochrome camera. For this purpose, the sample was illuminated with blue LEDs (465 nm). The 505-nm dichroic mirror was used
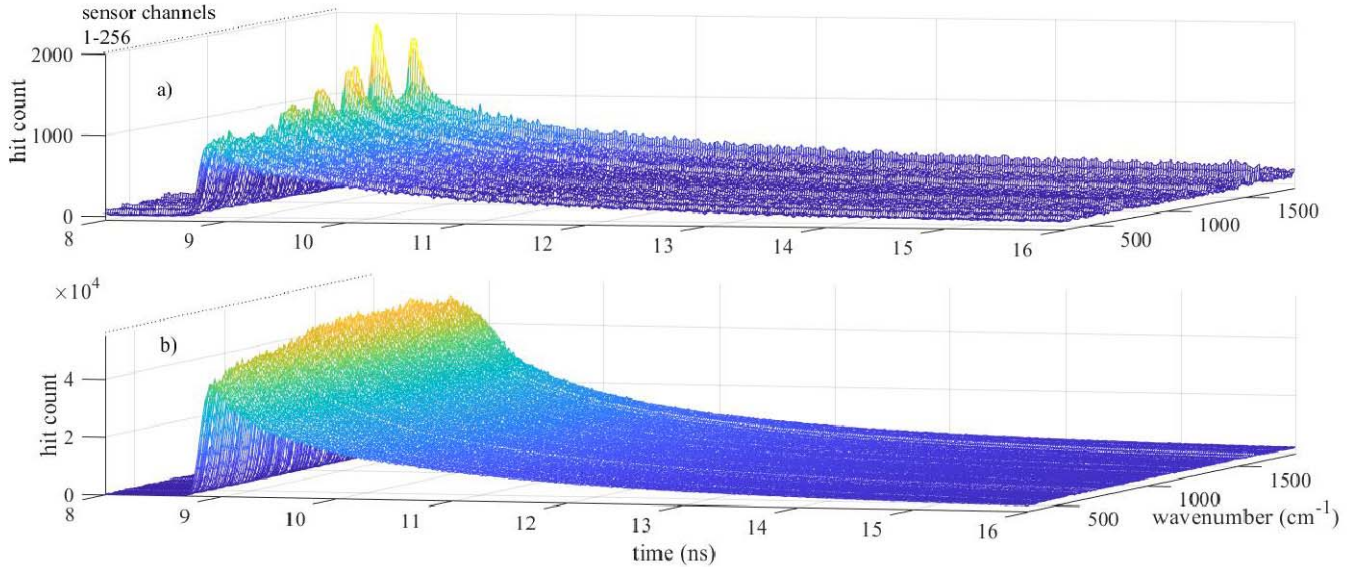
Fig. 2. Raw data from (a) organic sesame seed oil and (b) roasted sesame oil measurement for TDC bins 400–800.

to create a camera view based only on the blue LED illumination.

## III. CALIBRATION PROCEDURE AND MEASUREMENTS

The purpose of the calibration procedure is to characterize the timing skew along the line sensor. With the characterization data, a large share of spectral distortion caused by the timing skew can be eliminated in postprocessing.

The calibration procedure is based on the simple method for characterization of a line sensor described in [41]. In the calibration measurement, 20 million laser pulses were shot at the reference sample, an aqueous solution of erythrosin B (Sigma-Aldrich no. 198 269). The fluorescence lifetime of an aqueous solution of erythrosin B is short (89 ps) and wavelength range of its fluorescence emission is sufficient to cover the spectral range of the spectrometer [42]. Thus, the measurement of erythrosine B is a fast way to produce approximations of instrument response functions (IRFs) for all detector channels. For each channel, a polynomial was fitted to a result histogram and the vertex of the polynomial was used to determine a channel-specific timestamp. Timestamp values in TDC bin numbers were multiplied by nominal TDC resolution (20 ps) to convert the timestamps into picosecond scale. Timestamps as a function of channel number indicate the shape of the timing skew of the sensor and they can be used for skew compensation as described in [41].

The accuracy of this simple characterization method can be improved without any additional measurements. The principal idea behind the improvement is that the spectrum of the reference sample erythrosin B consists of fluorescence and should not include sharp peaks. The fluorescence emission spectrum of erythrosin B can be found in [43]. Thus, all sharp peaks in the spectrum of the reference sample are assumed to be related to distortion caused by timing skew, and timing skew characterization data can be adjusted to minimize distortion peaks. In practice, this idea was applied as follows. First, the spectrum of the reference sample was calculated using timing skew compensation based on timestamps from the calibration measurement. Photon counts from bins 432–440 with the addition of channel-specific compensation terms were used. As an example, sensor channel number 218 is studied. The timestamp value was 50.7 ps for channel number 218. When compared with the nominal temporal resolution of the TDC, 20, 50.7 ps corresponds to two full bins and about one half. Now the channel-specific compensation term for channel number 218 is $N_{441,218} + N_{442,218} + (10.7\,\text{ps})/(20\,\text{ps})N_{443,218}$, where $N_{a,b}$ is photon count for TDC bin a in sensor channel b. This compensation term is added to sum $N_{432,218} + N_{433,218} + \cdots + N_{440,218}$ to calculate the skew-compensated photon count for channel number 218. When the skew-compensated photon counts for all channels were calculated, the spectrum of the reference sample was formed, as shown in Fig. 3(a) (black line). Next, a smooth undistorted version of the spectrum of reference sample was created using moving average filtering. Then, a comparison was made between the filtered and unfiltered spectrum to detect residual distortion caused by timing skew. Based on the comparison, the original timestamps were adjusted to minimize differences between filtered and unfiltered spectrum. Finally, all steps needed to adjust the timestamps were repeated two times to iteratively make timestamps as accurate as possible. For channel number 218, timestamp was adjusted approximately $-0.1$ ps after iterations and, therefore, final adjusted timestamp was 50.7 ps $-$ 0.1 ps $=$ 50.6 ps, as shown in Fig. 3(b).

The final adjusted timestamps shown in Fig. 3(b) (black line) describe the timing skew of the sensor. The differences between the adjacent channels are in the range of 0–24 ps and the maximum difference is observed between channels number 1 and 256, amounting for 86 ps in total. The sum of adjustments made to the timestamps during iterations is also shown in Fig. 3(b) as blue line. The adjustments are small, in the range of ±3 ps, but their effect on the spectrum of the reference sample is clear in Fig. 3(a) (blue line).
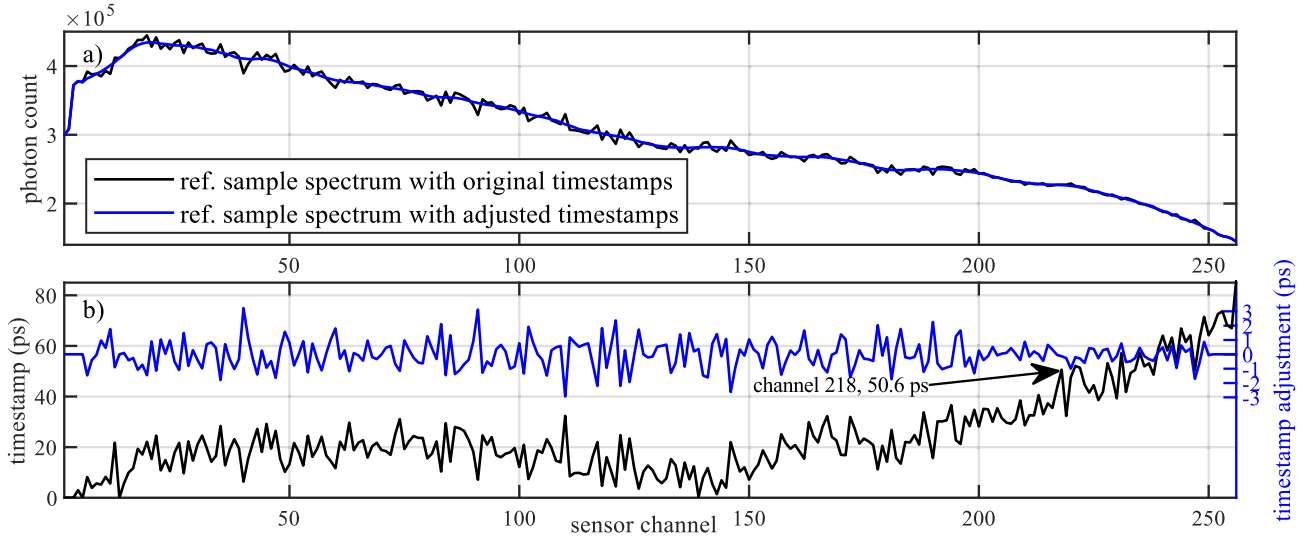
Fig. 3. (a) Spectrum of the reference sample calculated using skew compensation with original timestamps (black line) and using skew compensation with adjusted more accurate timestamps (blue line). (b) Shape of the timing skew of the sensor based on the improved characterization method (black line) and adjustments made to original timestamps based on the spectrum of the reference sample (blue line).

## IV. MEASUREMENTS AND DATA POSTPROCESSING

### A. Measured Samples

Two oil samples were measured to assess the performance of the spectrometer. The first sample was organic sesame seed oil having a CW fluorescence-to-Raman ratio of 10.5 and a fluorescence lifetime of 2.7 ns. The second, significantly more challenging, sample was roasted sesame seed oil having a CW fluorescence-to-Raman ratio of 82 and a fluorescence lifetime of 2.2 ns. These values were determined from the same data that were used to calculate the spectra of oils (shown in Fig. 2). The Raman spectra of edible oils including sesame seed oil can be found in [44]. For CW fluorescence-to-Raman ratios, fluorescence levels were calculated as a sum of fluorescence photons detected in a 15-ns period after the laser pulse at 1500 cm$^{-1}$ (no Raman peak) and Raman levels were taken from the largest Raman peak at 1440 cm$^{-1}$ using 600-ps time gating. Due to the weak Raman signal level, CW fluorescence-to-Raman ratios for small Raman peak at 1750 cm$^{-1}$ are difficult to calculate accurately but approximated values are 90 for organic sesame seed oil and 560 for roasted sesame seed oil (the Raman peak at 1750 cm$^{-1}$ was compared with the fluorescence level at 1700 cm$^{-1}$ (no Raman peak) instead of 1500 cm$^{-1}$). A gate width of 600 ps was chosen to include all Raman photons while still rejecting most of the fluorescence. The fluorescence lifetimes were determined by fitting a single exponential model to the fluorescence decay using data from sensor channel 200 ($\sim$1500 cm$^{-1}$). Two million laser pulses were shot at the organic sesame seed oil (duration $\sim$29 s) and ten million laser pulses were shot at the roasted sesame seed oil ($\sim$143 s).

To compare 573-nm excitation with more common 532-nm excitation, organic sesame seed oil sample was also measured using another pulsed laser, Teem Photonics ANG-500P-CHS. With 532-nm excitation, the CW fluorescence-to-Raman ratio of the Raman peak at 1440 cm$^{-1}$ was 39.4 which is significantly higher than 10.5 observed with 573-nm excitation.

### B. IRF Measurement

To estimate the IRF of the spectrometer, a paracetamol sample was measured. The widths of photon distributions on channels 86, 166, and 219 were 149, 155, and 152 ps (FWHM), respectively. The photon distribution of channel 219 is shown in Fig. 4. The selected channels correspond to largest Raman peaks of paracetamol at 857, 1322, and 1609 cm$^{-1}$. Based on channels 86, 166, and 219, the FWHM of IRF of the spectrometer averages to 152 ps. Even though the fluorescence emission from paracetamol is weak, it may cause a small overestimation in the IRF FWHM value. This effect was neglected. The dominant factors for the IRF FWHM value are the laser pulsewidth and the jitter of SPADs which have maximum values of approximately 100 ps (FWHM).

### C. Raman Measurements and Postprocessing

Before creating any spectra, a simple correction for pile-up distortion defined in (1) was applied to the data. The corrected photon count for TDC bin $a$ in sensor channel $b$, $N_{a,b}$, is

$$N_{a,b} = n_{a,b} \frac{m}{m - \sum_{i=1}^{a-1} n_{i,b}} \tag{1}$$

where $n_{a,b}$ is detected photon count for TDC bin $a$ in sensor channel $b$ and $m$ is the total number of laser pulses shot.

The width of the chosen time gate affects the spectrum in multiple ways. In many cases, the best signal-to-noise ratio in terms of shot noise is achieved when almost all Raman photons are included. Unfortunately, the time gate endpoint is then set to a level having approximately maximum overall signal intensity meaning maximum distortion caused by timing skew. This tradeoff is illustrated in Fig. 5. The effect of timing skew can be reduced if the endpoint of time gate is shifted to a level having a lower overall signal but then some Raman photons are lost (for shorter gate) or the number of included fluorescence photons is increased (for wider gate). If spectral distortion is mainly caused by timing skew, it may be best to set the time gate endpoint to most accurately characterized
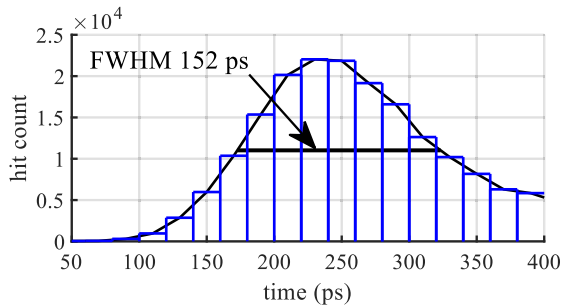
Fig. 4. Photon distribution of IRF measurement (paracetamol) at 1609 cm$^{-1}$ (sensor channel 219).
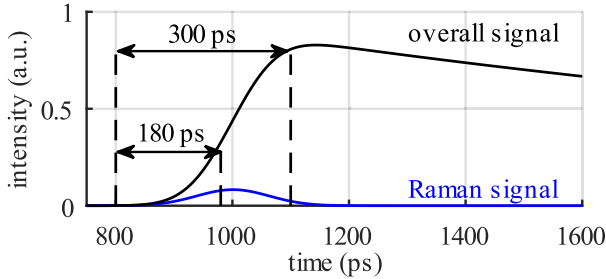


Fig. 5. Gate width examples to maximize included Raman photons (300 ps) or to minimize distortion caused by timing skew (180 ps).

level of the TDC's range to maximize the efficiency of timing skew compensation. So, the optimal gate width is a compromise, with both sensor and sample have an effect on it. Gate width used to calculate spectra in Figs. 6 and 7 is approximately 200 ps. Such gating resembles the 180-ps example shown in Fig. 5 and 40%–45% of Raman photons are included with it. This gate width is chosen primarily to maximize the efficiency of timing skew compensation because timing skew is the dominant error source if highly fluorescent samples are measured with this sensor.

Multiple postprocessing steps are needed to minimize spectral distortion caused by dark counts and timing skew of the sensor. As the dominant source of spectral distortion depends on the measured sample, the importance of each postprocessing step varies when different kinds of samples are measured. To illustrate the effect of each postprocessing step, five spectra are shown for both oil samples. Spectra related to organic sesame seed oil are shown in Fig. 6 and spectra related to roasted sesame seed oil are shown in Fig. 7. The spectral range covered in the measurements was 247–1826 cm$^{-1}$, but the range shown in Figs. 6 and 7 is 600–1800 cm$^{-1}$, because it is the most relevant part for the oil samples. Raw spectra in Figs. 6(a) and 7(a) are calculated simply by summing photon counts of TDC bins 432–441 in all channels. In practice, this means time gating with a gate width of 200 ps. In the raw spectrum of organic sesame seed oil in Fig. 6(a), distortion is visible but large Raman peaks can still be seen clearly. In the raw spectrum of roasted sesame oil in Fig. 7(a), Raman peaks can hardly be seen because of overwhelming distortion.

For dark count compensation, the DCR of each channel was estimated using hit counts from TDC bins 2200–2800. This period is located more than 30 ns after the excitation pulse and, therefore, only dark counts are assumed to be detected there. When dark counts were compensated, the spectral

quality of organic sesame seed oil [Fig. 6(a)] improved noticeably, while distortion in the spectrum of roasted sesame seed oil [Fig. 7(a)] decreased only marginally. However, this difference is not related to different DCRs but results from different levels of distortion caused by timing skew due to different fluorescence levels.

Timing skew compensation was implemented as described in Section III for the calibration sample. Again, photon counts from bins 432–440 with the addition of channel-specific compensation terms were used. Blue lines in Figs. 6(b) and 7(b) are spectra calculated with the skew compensation using unadjusted timestamps, like described in [41]. Black lines in Figs. 6(b) and 7(b) are spectra calculated with the improved skew compensation using adjusted timestamps shown in Fig. 3. Timing skew compensation reduces spectral distortion for both oil samples, and especially for roasted sesame seed oil, its importance is notable. For organic sesame seed oil, there are no large differences in the two spectra in Fig. 6(b) but for roasted sesame seed oil, improved skew compensation eliminates spectral distortion more effectively, as shown in Fig. 7(b). Small adjustments ($\pm 3$, $\pm 2$ ps for most channels) in the characterization of the sensor make visible difference to the spectrum of roasted sesame oil showing how sensitive time-gated measurement is to timing skew when highly fluorescent samples having short fluorescence lifetime are measured. It should be noted that the improved iterative skew compensation should be used only when timing skew of the sensor really is the dominant source of distortion.

Finally, for spectra shown in Figs. 6(c) and 7(c), baseline correction and computational filtering were applied. The baseline was created by fitting a curve through points known not to have Raman peaks and filtering was implemented using the smoothdata function in MATLAB (smoothing method "sgolay," window length 5, and degree of the polynomial 2). After all postprocessing steps, the Raman peaks at 1080, 1265, 1300, 1440, 1660, and 1750 cm$^{-1}$ are clearly visible for both oil samples.

### D. Evaluation of Measurement Results

Hit counts and fluorescence-to-Raman ratios for the time-gated measurements are shown in Table I. These ratios were calculated using the largest Raman peak at 1440 cm$^{-1}$ and the fluorescence level at 1500 cm$^{-1}$ as per the ratios calculated for the CW-mode in Section IV-A. Table I shows that if time-gated measurements are compared with CW-mode measurements presented in Section IV-A, the number of detected Raman photons is decreased approximately 60%, while the number of detected fluorescence photons decreases more than 98%. Therefore, the fluorescence-to-Raman ratio of time-gated measurement is only about 4% of the fluorescence-to-Raman ratio of CW-mode measurement.

To estimate the significance of the postprocessing steps, spectral distortion values for each step were collected to Table II. The distortion levels were calculated as a standard deviation of the baseline-corrected hit counts over the range of 1500–1621 cm$^{-1}$ [sensor channels 198–220, shown in Fig. 7(c)], which does not include Raman peaks. Distortion levels in Table II are normalized so that the level
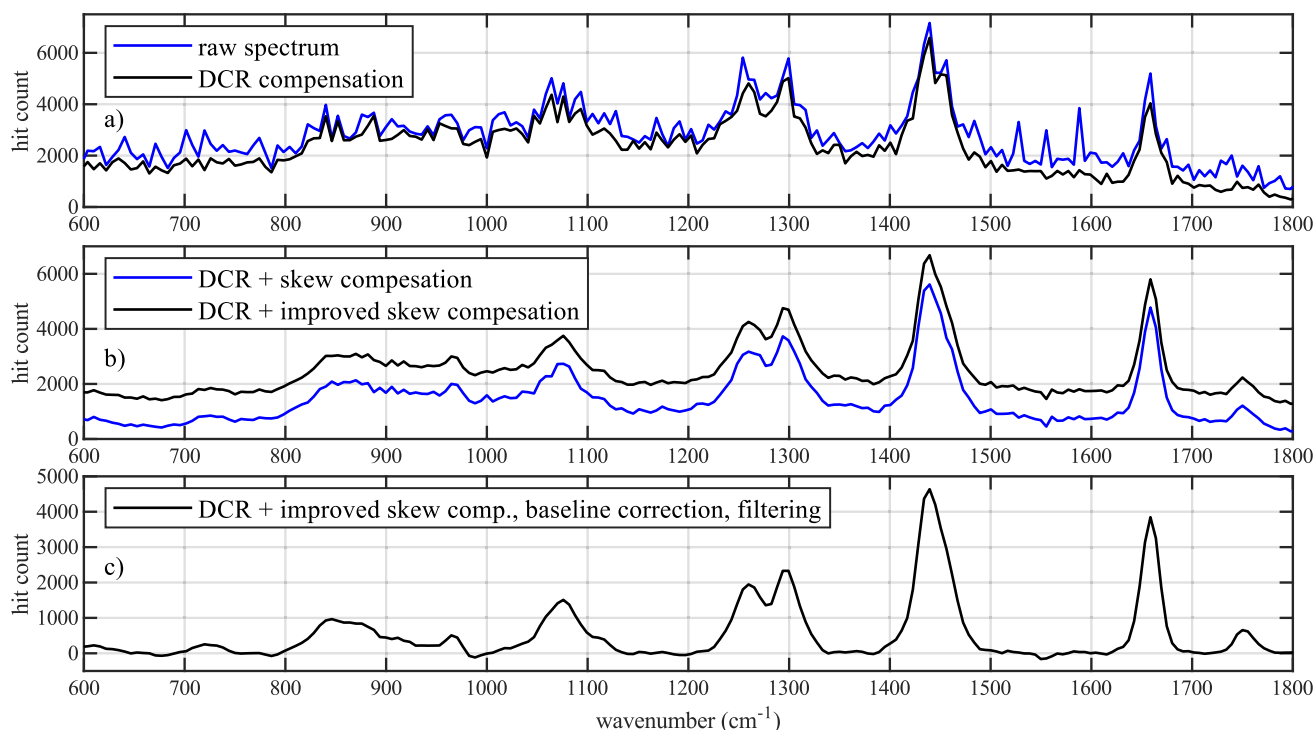
Fig. 6. Spectra of organic sesame seed oil after different postprocessing steps. (a) No postprocessing with the exception of pile-up distortion correction (blue line) and dark count compensation applied (black line). (b) Dark count compensation and skew compensation applied, and blue line shifted down for clarity. (c) Dark count compensation, skew compensation, baseline correction, and filtering applied.
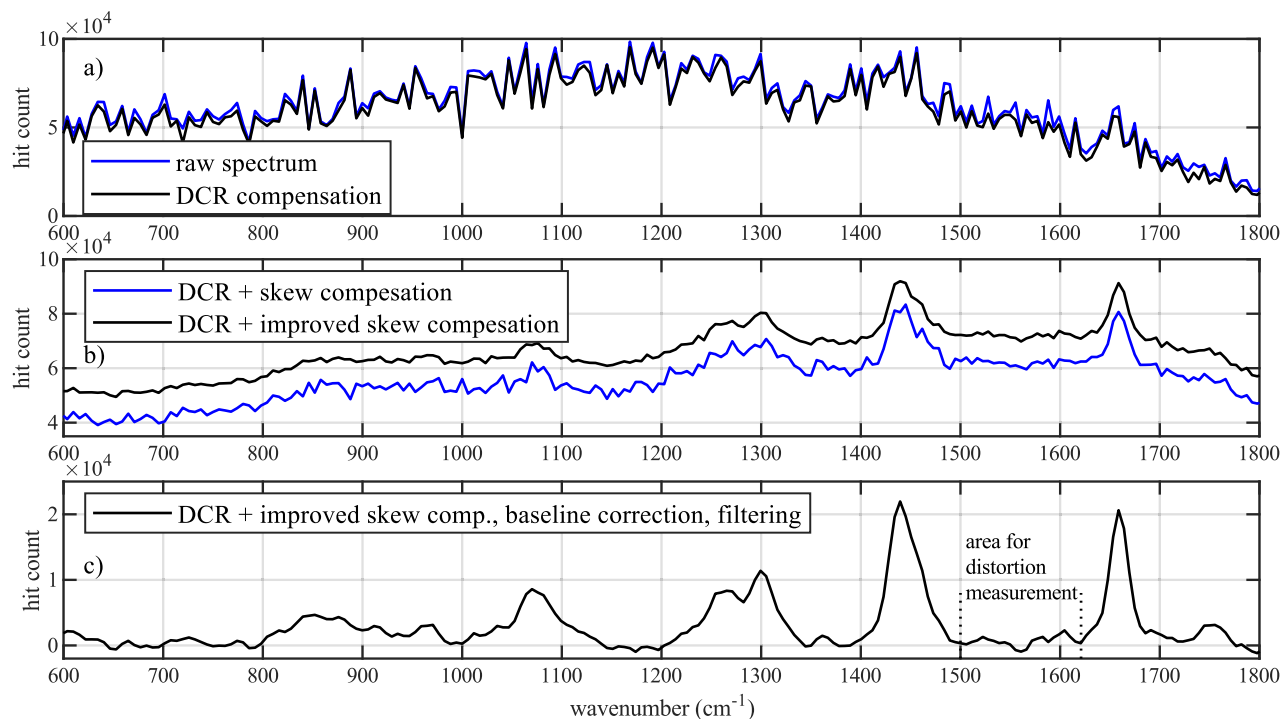


Fig. 7. Spectra of roasted sesame seed oil after different postprocessing steps. (a) No postprocessing with the exception of pile-up distortion correction (blue line) and dark count compensation applied (black line). (b) Dark count compensation and skew compensation applied, and blue line shifted down for clarity. (c) Dark count compensation, skew compensation, baseline correction, and filtering applied.

of the raw spectrum equals one. For organic sesame seed oil, dark counts cause most of the distortion and DCR compensation alone reduces the distortion level by 79%. For this sample, the importance of timing skew compensation is minimal and computational filtering can be used for some additional reduction in distortion level. For highly fluorescent roasted sesame seed oil, DCR compensation

reduces the distortion level only by 17%, while timing skew compensation together with DCR compensation is able to reduce distortion level by 87%. A small additional reduction can be achieved with computational filtering. For roasted sesame seed oil, the combination of DCR compensation and filtering was not very effective without timing skew compensation.

TABLE I
HIT COUNTS AND F/R RATIOS FOR CW-MODE AND TIME-GATED MEASUREMENT

| Sample | CW-mode | | | Time-gated (gate width 200 ps) | | | |
|---|---|---|---|---|---|---|---|
| | Fluorescence hit count | Raman hit count | F/R ratio (CW) | Fluorescence hit count | Raman hit count | F/R ratio (TG) | $F/R_{CW} / F/R_{TG}$ |
| Organic | 112300 | 10500 | 10.7 | 2050 | 4600 | 0.45 | 24.0 |
| Roasted | 4484000 | 54100 | 82.9 | 71850 | 21650 | 3.32 | 25.0 |

TABLE II
NORMALIZED SPECTRAL DISTORTION LEVELS AFTER DIFFERENT
POSTPROCESSING STEPS

| Sample | Post-processing | | | | |
|---|---|---|---|---|---|
| | RAW | DCR | DCR & skew comp. | DCR, skew comp. & filtering | DCR & filtering, no skew comp. |
| Organic | 1 | 0.21 | 0.20 | 0.12 | 0.13 |
| Roasted | 1 | 0.83 | 0.13 | 0.11 | 0.48 |

The spectral quality of the fully postprocessed spectra was also quantitatively measured using the signal-to-distortion ratio (SDR) described in [29]. The distortion level was again calculated as a standard deviation of hit counts over the range of 1500–1621 cm$^{-1}$, and the highest hit count of the Raman peak was used as a signal level. SDR values for the largest Raman peak at 1440 cm$^{-1}$ are 28.2 and 76.2 for roasted and organic sesame seed oil, respectively. For significantly smaller Raman peak at 1750 cm$^{-1}$, SDR values are 3.1 (roasted oil) and 10.8 (organic oil).

## V. CONCLUSION

A time-resolved Raman spectrometer was designed based on a 256-channel CMOS SPAD line sensor and a 573-nm high-energy pulsed laser. A high fluorescence rejection was mainly achieved by means of time gating due to short (sub-100-ps FWHM) laser pulse excitation and good temporal resolution (20 ps) of the sensor. Time gating improved the fluorescence-to-Raman ratio of both the measured sesame seed oils by a factor of 24–25. Excitation at 573 nm proved to be a good choice at least for oil samples; for organic sesame seed oil, fluorescence-to-Raman ratio was 73% lower at 573-nm excitation than with typical 532-nm excitation. The presented calibration and postprocessing steps removed almost 90% of spectral distortion caused by dark counts and timing skew of the sensor. If DCR and timing skew of the sensor could be further reduced in future sensor designs, less complicated postprocessing procedure might be effective. Regarding the laser used in this spectrometer, the most obvious feature to be improved is the 70-kHz pulse rate. Recent CMOS SPAD line sensors can usually handle pulse rates significantly higher than 70 kHz and, therefore, the pulse rate of the laser limits the measurement speed and increases the measurement times.

CMOS SPAD-based time-resolved Raman spectrometers have already been successfully applied to mineral identification and chemical imaging of human teeth, for example. In both cases, fluorescence suppression due to time gating has been appropriate, but the timing skew of the line sensor has been one of the main factors limiting the performance of the spectrometer [28], [45]. The obtained results are important, because they show that with a well-designed line sensor and suitable postprocessing steps, the effective timing skew can

be pushed from tens of picoseconds to picosecond level. In addition, with the available pulsed diamond Raman lasers, the excitation wavelength can be chosen to optimize the fluorescence rejection of the spectrometer for a certain kind of samples, as demonstrated with the oil samples. In addition, the time-resolved Raman spectrometer technology developed here could pave the way for the development of a practical device for medicine, where the high fluorescence background of blood cells could be effectively rejected by utilizing a proper available 620-nm wavelength of a pulsed diamond Raman laser with the accurate time-resolved CMOS SPAD line sensor. Overall, the achieved good spectral quality for challenging fluorescent samples encourages to apply CMOS SPAD-based time-resolved Raman spectroscopy to more and more wide range of applications.

## REFERENCES

[1] G. C. Green, A. D. C. Chan, B. S. Luo, H. Dan, and M. Lin, "Identification of listeria species using a low-cost surface-enhanced Raman scattering system with wavelet-based signal processing," *IEEE Trans. Instrum. Meas.*, vol. 58, no. 10, pp. 3713–3722, Oct. 2009, doi: 10.1109/TIM.2009.2019317.

[2] Á. L. Gallego, A. R. Guesalaga, E. Bordeu, and Á. S. Gonzalez, "Rapid measurement of phenolics compounds in red wine using Raman spectroscopy," *IEEE Trans. Instrum. Meas.*, vol. 60, no. 2, pp. 507–512, Feb. 2011, doi: 10.1109/TIM.2010.2051611.

[3] P. Escarate, A. R. Guesalaga, V. R. Albertini, and D. Bailo, "Assessment of three spectroscopic techniques for rapid estimation of calcite in copper ore," *IEEE Trans. Instrum. Meas.*, vol. 59, no. 7, pp. 1911–1917, Jul. 2010, doi: 10.1109/TIM.2009.2028774.

[4] M.-Q. Zou *et al.*, "Rapid authentication of olive oil adulteration by Raman spectrometry," *J. Agricul. Food Chem.*, vol. 57, no. 14, pp. 6001–6006, Jul. 2009, doi: 10.1021/jf900217s.

[5] S. R. Khandasammy *et al.*, "Bloodstains, paintings, and drugs: Raman spectroscopy applications in forensic science," *Forensic Chem.*, vol. 8, pp. 111–133, May 2018, doi: 10.1016/j.forc.2018.02.002.

[6] K. Kong, C. Kendall, N. Stone, and I. Notingher, "Raman spectroscopy for medical diagnostics—From in-vitro biofluid assays to *in-vivo* cancer detection," *Adv. Drug Del. Rev.*, vol. 89, pp. 121–134, Jul. 2015, doi: 10.1016/j.addr.2015.03.009.

[7] Z. Liu *et al.*, "Raman spectroscopy for the discrimination and quantification of fuel blends," *J. Raman Spectrosc.*, vol. 50, no. 7, pp. 1008–1014, Apr. 2019, doi: 10.1002/jrs.5602.

[8] D. Bersani and P. P. Lottici, "Raman spectroscopy of minerals and mineral pigments in archaeometry," *J. Raman Spectrosc.*, vol. 47, no. 5, pp. 499–530, May 2016, doi: 10.1002/jrs.4914.

[9] G. Fini, "Applications of Raman spectroscopy to pharmacy," *J. Raman Spectrosc.*, vol. 35, no. 5, pp. 335–337, May 2004, doi: 10.1002/jrs.1161.

[10] B. Sharma, R. R. Frontiera, A. I. Henry, E. Ringe, and R. P. van Duyne, "SERS: Materials, applications, and the future," *Mater. Today*, vol. 15, nos. 1–2, pp. 16–25, 2012, doi: 10.1016/S1369-7021(12)70017-2.

[11] B. Robert, "Resonance Raman spectroscopy," *Photosynthesis Res.*, vol. 101, nos. 2–3, pp. 147–155, Sep. 2009, doi: 10.1007/s11120-009-9440-4.

[12] E. B. Hanlon *et al.*, "Prospects for *in vivo* Raman spectroscopy," *Phys. Med. Biol.*, vol. 45, no. 2, pp. R1–R59, Feb. 2000, doi: 10.1088/0031-9155/45/2/201.

[13] K. Bhatt, S. Tan, S. Karumuri, and A. K. Kalkan, "Charge-selective Raman scattering and fluorescence quenching by 'nanometal on semiconductor' substrates," *Nano Lett.*, vol. 10, no. 10, pp. 3880–3887, Oct. 2010, doi: 10.1021/nl101480n.

[14] K. Golcuk, G. S. Mandair, A. F. Callender, N. Sahar, D. H. Kohn, and M. D. Morris, "Is photobleaching necessary for Raman imaging of bone tissue using a green laser?" *Biochimica Biophys. Acta*, vol. 1758, no. 7, pp. 868–873, Jul. 2006, doi: 10.1016/j.bbamem.2006.02.022.

[15] P. Simon *et al.*, "High temperatures and Raman scattering through pulsed spectroscopy and CCD detection," *J. Raman Spectrosc.*, vol. 34, nos. 7–8, pp. 497–504, Jul. 2003, doi: 10.1002/jrs.1020.

[16] P. Matousek *et al.*, "Fluorescence suppression in resonance Raman spectroscopy using a high-performance picosecond kerr gate," *J. Raman Spectrosc.*, vol. 32, no. 12, pp. 983–988, Dec. 2001, doi: 10.1002/jrs.784.

[17] R. P. Van Duyne, D. L. Jeanmaire, and D. F. Shriver, "Mode-locked laser Raman spectroscopy. New technique for the rejection of interfering background luminescence signals," *Anal. Chem.*, vol. 46, no. 2, pp. 213–222, Feb. 1974, doi: 10.1021/ac60338a012.

[18] J. Blacksberg, G. R. Rossman, and A. Gleckler, "Time-resolved Raman spectroscopy for *in situ* planetary mineralogy," *Appl. Opt.*, vol. 49, no. 26, p. 4951, Sep. 2010, doi: 10.1364/AO.49.004951.

[19] J. Kostamovaara, J. Tenhunen, M. Kögler, I. Nissinen, J. Nissinen, and P. Keränen, "Fluorescence suppression in Raman spectroscopy using a time-gated CMOS SPAD," *Opt. Exp.*, vol. 21, no. 25, p. 31632, Dec. 2013, doi: 10.1364/oe.21.031632.

[20] I. Nissinen, J. Nissinen, P. Keränen, and J. Kostamovaara, "On the effects of the time gate position and width on the signal-to-noise ratio for detection of Raman spectrum in a time-gated CMOS single-photon avalanche diode based sensor," *Sens. Actuators B, Chem.*, vol. 241, pp. 1145–1152, Mar. 2017, doi: 10.1016/j.snb.2016.10.021.

[21] A. T. Erdogan *et al.*, "A CMOS SPAD line sensor with per-pixel histogramming TDC for time-resolved multispectral imaging," *IEEE J. Solid-State Circuits*, vol. 54, no. 6, pp. 1705–1719, Jun. 2019, doi: 10.1109/JSSC.2019.2894355.

[22] Y. Maruyama, J. Blacksberg, and E. Charbon, "A 1024 ×8, 700-ps time-gated SPAD line sensor for planetary surface exploration with laser Raman spectroscopy and LIBS," *IEEE J. Solid-State Circuits*, vol. 49, no. 1, pp. 179–189, Jan. 2014, doi: 10.1109/JSSC.2013.2282091.

[23] I. Nissinen, J. Nissinen, P. Keranen, D. Stoppa, and J. Kostamovaara, "A 16 × 256 SPAD line detector with a 50-ps, 3-bit, 256-channel time-to-digital converter for Raman spectroscopy," *IEEE Sensors J.*, vol. 18, no. 9, pp. 3789–3798, May 2018, doi: 10.1109/JSEN.2018.2813531.

[24] M. Moreno-Garcia, H. Xu, L. Gasparini, and M. Perenzoni, "Low-noise single photon avalanche diodes in a 110 nm CIS technology," in *Proc. Eur. Solid-State Device Res. Conf.*, Sep. 2018, pp. 94–97, doi: 10.1109/ESSDERC.2018.8486883.

[25] M.-J. Lee, P. Sun, and E. Charbon, "A first single-photon avalanche diode fabricated in standard SOI CMOS technology with a full characterization of the device," *Opt. Exp.*, vol. 23, no. 10, p. 13200, May 2015, doi: 10.1364/oe.23.013200.

[26] H. Xu, L. Pancheri, G.-F.-D. Betta, and D. Stoppa, "Design and characterization of a p+/n-well SPAD array in 150nm CMOS process," *Opt. Exp.*, vol. 25, no. 11, p. 12765, May 2017, doi: 10.1364/oe.25.012765.

[27] E. A. G. Webster, L. A. Grant, and R. K. Henderson, "A high-performance single-photon avalanche diode in 130-nm CMOS imaging technology," *IEEE Electron Device Lett.*, vol. 33, no. 11, pp. 1589–1591, Nov. 2012, doi: 10.1109/LED.2012.2214760.

[28] J. Blacksberg, E. Alerstam, C. J. Cochrane, Y. Maruyama, and J. D. Farmer, "Miniature high-speed, low-pulse-energy picosecond Raman spectrometer for identification of minerals and organics in planetary science," *Appl. Opt.*, vol. 59, no. 2, p. 433, Jan. 2020, doi: 10.1364/ao.59.000433.

[29] J. Kekkonen, T. Talala, J. Nissinen, and I. Nissinen, "On the spectral quality of time-resolved CMOS SPAD-based Raman spectroscopy with high fluorescence backgrounds," *IEEE Sensors J.*, vol. 20, no. 9, pp. 4635–4645, May 2020, doi: 10.1109/jsen.2020.2966119.

[30] A. Usai, N. Finlayson, C. D. Gregory, C. Campbell, and R. K. Henderson, "Separating fluorescence from Raman spectra using a CMOS SPAD TCSPC line sensor for biomedical applications," *Proc. SPIE Opt. Biopsy XVII, Real-Time Spectroscopic Imag. Diagnosis*, vol. 10873, Mar. 2019, Art. no. 108730R, doi: 10.1117/12.2508459.

[31] T. Rojalin *et al.*, "Fluorescence-suppressed time-resolved Raman spectroscopy of pharmaceuticals using complementary metal-oxide semiconductor (CMOS) single-photon avalanche diode (SPAD) detector," *Anal. Bioanal. Chem.*, vol. 408, no. 3, pp. 761–774, Jan. 2016, doi: 10.1007/s00216-015-9156-6.

[32] Z. G. Cerovic *et al.*, "The use of chlorophyll fluorescence excitation spectra for the non-destructive *in situ* assessment of UV-absorbing compounds in leaves," *Plant, Cell Environ.*, vol. 25, no. 12, pp. 1663–1676, Dec. 2002, doi: 10.1046/j.1365-3040.2002.00942.x.

[33] M. Zandomeneghi, L. Carbonaro, and C. Caffarata, "Fluorescence of vegetable oils: Olive oils," *J. Agricult. Food Chem.*, vol. 53, no. 3, pp. 759–766, Feb. 2005, doi: 10.1021/jf048742p.

[34] C. G. Atkins, K. Buckley, M. W. Blades, and R. F. B. Turner, "Raman spectroscopy of blood and blood components," *Appl. Spectrosc.*, vol. 71, no. 5, pp. 767–793, May 2017, doi: 10.1177/0003702816686593.

[35] Y. Y. Hui, L.-J. Su, O. Y. Chen, Y.-T. Chen, T.-M. Liu, and H.-C. Chang, "Wide-field imaging and flow cytometric analysis of cancer cells in blood by fluorescent nanodiamond labeling and time gating," *Sci. Rep.*, vol. 4, no. 1, May 2015, Art. no. 5574, doi: 10.1038/srep05574.

[36] G. Tomazzoni *et al.*, "Identification of vegetable oil or biodiesel added to diesel using fluorescence spectroscopy and principal component analysis," *J. Amer. Oil Chemists' Soc.*, vol. 91, no. 2, pp. 215–227, Feb. 2014, doi: 10.1007/s11746-013-2354-5.

[37] J. Nikkinen *et al.*, "Sub-100 ps monolithic diamond Raman laser emitting at 573 nm," *IEEE Photon. Technol. Lett.*, vol. 30, no. 11, pp. 981–984, Jun. 1, 2018, doi: 10.1109/LPT.2018.2806183.

[38] J. Nikkinen, A. Härkönen, and M. Guina, "Sub-50 ps pulses at 620 nm obtained from frequency doubled 1240 nm diamond Raman laser," *Opt. Exp.*, vol. 25, no. 24, p. 30365, Nov. 2017, doi: 10.1364/oe.25.030365.

[39] P. Keranen and J. Kostamovaara, "256 × 8 SPAD array with 256 column TDCs for a line profiling laser radar," *IEEE Trans. Circuits Syst. I, Reg. Papers*, vol. 66, no. 11, pp. 4122–4133, Nov. 2019, doi: 10.1109/TCSI.2019.2923263.

[40] P. Keranen and J. Kostamovaara, "256 × TDC array with cyclic interpolators based on calibration-free 2× time amplifier," *IEEE Trans. Circuits Syst. I, Reg. Papers*, vol. 66, no. 2, pp. 524–533, Feb. 2019, doi: 10.1109/TCSI.2018.2868242.

[41] T. Talala and I. Nissinen, "Timing skew compensation methods for CMOS SPAD line sensors used for Raman spectroscopy," in *Proc. IEEE SENSORS*, Oct. 2019, pp. 1–4, doi: 10.1109/SENSORS43011.2019.8956897.

[42] N. Boens *et al.*, "Fluorescence lifetime standards for time and frequency domain fluorescence spectroscopy," *Anal. Chem.*, vol. 79, no. 5, pp. 2137–2149, Mar. 2007, doi: 10.1021/ac062160k.

[43] L. S. Herculano *et al.*, "Photodegradation in micellar aqueous solutions of erythrosin esters derivatives," *Appl. Spectrosc.*, vol. 69, no. 7, pp. 883–888, Jul. 2015, doi: 10.1366/15-07865.

[44] W. Gong, R. Shi, M. Chen, J. Qin, and X. Liu, "Quantification and monitoring the heat-induced formation of trans fatty acids in edible oils by Raman spectroscopy," *J. Food Meas. Characterization*, vol. 13, no. 3, pp. 2203–2210, Sep. 2019, doi: 10.1007/s11694-019-00140-5.

[45] J. Kekkonen, M. A. J. Finnilä, J. Heikkilä, V. Anttonen, and I. Nissinen, "Chemical imaging of human teeth by a time-resolved Raman spectrometer based on a CMOS single-photon avalanche diode line sensor," *Analyst*, vol. 144, no. 20, pp. 6089–6097, Oct. 2019, doi: 10.1039/c9an01136f.

**Tuomo Talala** received the M.Sc. (Math) and M.Sc. (Tech.) degrees from the University of Oulu, Oulu, Finland, in 2010 and 2018, respectively, where he is currently pursuing the Ph.D. degree in electrical engineering with Circuits and Systems Research Unit.

His research interests include the development of integrated sensors and data postprocessing techniques for time-resolved Raman spectroscopy.

**Ville A. Kaikkonen** was born in Oulu, Finland. He received the M.Sc. (Tech.) degree in electrical engineering from the University of Oulu, Oulu, in 2010, where he is currently pursuing the D.Sc. (Tech.) degree in photonics.

He has been a Project Researcher with the University of Oulu, since 2010. His current research interests include optical measurement systems, especially Raman spectroscopy and digital holographic imaging applications.

**Pekka Keränen** (Member, IEEE) received the M.Sc. (Tech) and D.Sc. (Tech) degrees in electrical engineering from the University of Oulu, Oulu, Finland, in 2010 and 2016, respectively.

From 2008 to 2019, he was with the Circuits and Systems Research Unit, University of Oulu. Since 2019, he has been a Senior Analog IC Design Engineer with CoreHW, Oulu. His main research interests include integrated circuit design for pulsed time-of-flight laser radars, such as single-photon avalanche diode (SPAD)-based receiver circuits and time-to-digital converters.

**Jari Nikkinen** received the M.Sc. degree in engineering and the Ph.D. degree from the Technical University of Tampere, Tampere, Finland, in 2014 and 2017, respectively. His Ph.D. work was focused on light sources based on Q-switched microchip lasers.

After Ph.D., he has been working at Modulight Inc., Tampere, as a Device Engineer in laser diode production and Research and Development projects.

**Antti Härkönen** received the Ph.D. degree in technology from the Tampere University of Technology, Tampere, Finland, in 2008.

His research has focused on experimental work on pulsed and continuous-wave surface-normal semiconductor lasers vertical-external-cavity surface-emitting lasers (VECSELs), as well as Q-switched solid-state microchip lasers.

**Vasili G. Savitski** received the Engineering Diploma in optics from the Belarus National Technical University, Minsk, Belarus, in 1999 and the Ph.D. degree from the Institute of Physics, Minsk, in 2005 for work on the nonlinear optics of quantum dots in glasses.

He worked with the International Laser Center, Minsk, from 1999 to 2007 and with the Institute of Photonics, Glasgow, U.K., between 2008 and 2019. Currently, he is with the Fraunhofer Centre for Applied Photonics, Glasgow.
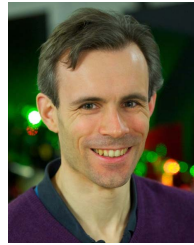
**Sean Reilly** received the M.Sci. degree in physics from the University of Strathclyde, Scotland, U.K., in 2011, and the Ph.D. degree from the Institute of Photonics, University of Strathclyde, in 2015 for work on the implementation and characterization of synthetic diamond as a laser material.

He continued to work with the Institute of Photonics as a Research Associate before moving to Coherent Scotland in 2017, where he currently works as a Laser Development Engineer.

**Łukasz Dziechciarczyk** received the M.Sc. degree in advanced applied electronics from the Wroclaw University of Technology, Wroclaw, Poland, in 2014, and the Ph.D. degree in nonlinear wavelength conversion using diamond from the University of Strathclyde, Glasgow, U.K., in 2020.

He spent two years for the extreme UV industry working on electro-optical device development and laser engineering. He is currently working in a laser company on the development of high power and tunable solid-state lasers.

**Alan J. Kemp** (Member, IEEE) received the B.Sc. degree (Hons.) from the University of Glasgow, Glasgow, U.K., in 1996 and the Ph.D. degree from the University of St. Andrews, St. Andrews, U.K., in 1999, for work on microchip lasers.

He worked on ultrafast lasers with the University of St. Andrews, from 1999 to 2002. In 2002, he moved to the Institute of Photonics, University of Strathclyde, Glasgow, U.K., where he works on solid-state laser engineering.

**Mircea Guina** (Member, IEEE) received the Ph.D. degree in physics from the Tampere University of Technology, Tampere, Finland, in 2002.

He is currently a Professor of semiconductor technology (optoelectronics), since 2008 and leads the Optoelectronics Research Centre team, a research group part of the Faculty of Engineering and Natural Sciences, Tampere University, Tampere. He conducts research on several major topics including molecular beam epitaxy of novel optoelectronic compounds, development of semiconductor lasers and high-efficiency solar cells, photonic integration, and use of lasers in medicine, light detection and ranging (LIDAR), and sensing. He has authored more than 200 journal articles, nine book chapters, has given more than 40 invited talks at major international conferences, and holds four international patents.

Dr. Guina has an outstanding track record in initiating and leading large-scale research projects extending from basic science to technology transfer. He is a current recipient of an European Research Council (ERC) Advanced Grant for the development of high efficiency solar cell technology (AMETIST). He is also Cofounder and Chairman of three start-ups related to laser technologies (Vexlum Oy, Reflekron Oy, and Picophotonics Oy). He is a Topical Editor for the *Optics Letters* journal and the *Journal of European Optical Society* and was awarded the Optical Society (OSA) Fellow and the Society of Photo-Optical Instrumentation Engineers (SPIE) Fellow distinctions for his work on optoelectronics and laser technologies.

**Anssi J. Mäkynen** received the M.Sc. (Tech.) (Hons.) and D.Sc. (Tech.) degrees from the University of Oulu, Oulu, Finland, in 1987 and 2000, respectively.

He is currently a Senior Research Fellow and a Research Group Leader with the Faculty of Information Technology and Electrical Engineering, University of Oulu. His current research interests include optical methods for industrial and environmental online inspection.

**Ilkka Nissinen** (Member, IEEE) received the M.Sc. (Eng.) and Dr.Tech. degrees in electrical engineering from the University of Oulu, Oulu, Finland, in 2002 and 2011, respectively.

Since 2018, he has been an Associate Professor of analog and mixed-signal microelectronic circuit design with the Circuits and Systems Research Unit, University of Oulu. His research interest includes the design of time interval measurement architecture for the integrated sensors of pulsed time-of-flight laser technologies.

Mr. Nissinen has been serving as a member for the Technical Program Committee of the IEEE Nordic Circuits and Systems Conference, since 2019.